

On chemiluminescent emission from an infiltrated chiral sculptured thin film

Siti S. Jamaian^a and Tom G. Mackay^{a,b,1}

^aSchool of Mathematics and Maxwell Institute for Mathematical Sciences,
University of Edinburgh, Edinburgh EH9 3JZ, UK

^bNanoMM—Nanoengineered Metamaterials Group, Department of Engineering Science and Mechanics,
Pennsylvania State University, University Park, PA 16802-6812, USA

Abstract

The theory describing the far-field emission from a dipole source embedded inside a chiral sculptured thin film (CSTF), based on a spectral Green function formalism, was further developed to allow for infiltration of the void regions of the CSTF by a fluid. In doing so, the extended Bruggeman homogenization formalism — which accommodates constituent particles that are small compared to wavelength but not vanishingly small — was used to estimate the relative permittivity parameters of the infiltrated CSTF. For a numerical example, we found that left circularly polarized (LCP) light was preferentially emitted through one face of the CSTF while right circularly polarized (RCP) light was preferentially emitted through the opposite face, at wavelengths within the Bragg regime. The centre wavelength for the preferential emission of LCP/RCP light was red shifted as the refractive index of the infiltrating fluid increased from unity, and this red shift was accentuated when the size of the constituent particles in our homogenization model was increased. Also, the bandwidth of the preferential LCP/RCP emission regime decreased as the refractive index of the infiltrating fluid increased from unity.

Keywords: Inverse Bruggeman homogenization formalism; spectral Green function; dipole radiation

1 Introduction

Chiral sculptured thin films (CSTFs) constitute a remarkable class of engineered materials. A CSTF comprises an array of parallel helical nanowires which can be grown on a substrate using vapour deposition techniques [1, 2]. By careful control of the fabrication process, both the optical properties and the multi-scale porosity of the CSTF can be tailored to order [3]. Accordingly, CSTFs are promising candidates as platforms for optical sensing, as well as a host of other applications [4, 5, 6].

Three quite different methods of utilizing CSTFs for optical sensing applications have been proposed. The first relies on the circular Bragg phenomenon, which CSTFs exhibit just as cholesteric liquid crystals do [7]. That is, within a wavelength regime known as the Bragg regime, a structurally right-handed CSTF almost completely reflects normally-incident right circularly polarized (RCP) plane waves whereas normally-incident left circularly polarized (LCP) plane waves are reflected very little. And vice versa for a structurally left-handed CSTF. The spectral shift in the circular Bragg phenomenon induced by infiltration of the void regions between the CSTF's nanowires may be exploited for sensing applications [8]. The second sensing

¹Email: T.Mackay@ed.ac.uk

methodology is based on the excitation of surface–plasmon–polariton waves at the interface of an infiltrated CSTF and a suitable metal [9]. The third methodology for CSTF–based optical sensing — which provides the main motivation for the present communication — involves the emission of radiation from a chemiluminescent source embedded within a CSTF [10].

Chemiluminescent radiation may be generated within a CSTF — and harnessed for optical biosensing — as follows. Suppose that certain biorecognition sites are immobilized on the surface of a CSTF’s nanowires, and the CSTF becomes infiltrated with a solution containing complementary analyte biomolecules. The binding of the analytes to the biorecognition sites, perhaps in the presence of a transition metal complex, results in the generation of chemiluminescent photons [11, 12]. For example, the biorecognition sites and the analytes could be fragments of complementary single–stranded DNA, which combine to produce chemiluminescence in the presence of a ruthenium complex [13, 14, 15]. Inspired by the prospects of this chemiluminescent sensing scenario, the theory of emission from a dipole source embedded inside a CSTF was recently established [16]. In the following, we extend the theory in order to investigate the effects on infiltration upon the far–field dipole radiation.

As regards notation, vectors and matrixes are represented in boldface, with the Cartesian unit vectors given by $\mathbf{u}_{x,y,z}$; dyadics are double–underlined; and both 4–vectors and 4×4 matrixes are enclosed within square brackets. The inverse of matrix $[\mathbf{Z}]$ is written as $[\mathbf{Z}]^{-1}$, while the inverse, adjoint and trace of the dyadic $\underline{\underline{Z}}$ are written as $\underline{\underline{Z}}^{-1}$, $\underline{\underline{Z}}^{adj}$ and $\text{tr}(\underline{\underline{Z}})$, respectively. The permittivity and the permeability of free space are denoted by ϵ_0 and μ_0 , respectively; $k_0 = \omega\sqrt{\epsilon_0\mu_0}$ is the free–space wavenumber; $\lambda_0 = 2\pi/k_0$ is the free–space wavelength; and $\eta_0 = \sqrt{\mu_0/\epsilon_0}$ is the intrinsic impedance of free space. An $\exp(-i\omega t)$ time–dependence is implicit, with ω being the angular frequency.

2 Theory

In this section we present an overview of the theory which describes the emission of electromagnetic radiation from a dipole source embedded inside a CSTF that is infiltrated by a fluid of refractive index n_ℓ . The theory rests upon two recently–established pillars: First, in §2.1 we describe how the constitutive parameters of an infiltrated CSTF can be estimated using an inverse homogenization technique. Second, in §2.2 the far–field radiative emission from a dipole source embedded in an infiltrated CSTF is estimated via a spectral Green function approach. Comprehensive details of these two pillars are available elsewhere [8, 16, 17]. Let us note that the theory presented in §2.1 represents an extension of that presented in [8] insofar as here the *extended* Bruggeman homogenization formalism is implemented. Also, the theory presented in §2.2 differs from that developed in [16] insofar as here we consider an *infiltrated* CSTF whose upper surface is immersed in a fluid of refractive index n_ℓ . A schematic diagram of the scenario under consideration is provided in Fig. 1.

2.1 Constitutive parameters of an infiltrated CSTF

A CSTF consists of an array of parallel nanowires. The ‘chirality’ of the CSTF stems from the fact that the nanowires are helical [1]. Such structures can be grown on a planar substrate — parallel to the plane $z = 0$, say — by the deposition of an evaporated bulk material. The helical shape of the nanowires is achieved by means of uniform rotation of the substrate about the z axis during the deposition process. We suppose that the deposited material is an isotropic dielectric material of refractive index n_s . Notice that the value of n_s needs to be determined as it may differ somewhat from the refractive index of the bulk material that was evaporated, depending upon the precise nature of the deposition conditions [18, 19, 20].

It is convenient here to regard the individual helices of a CSTF as strings of highly elongated ellipsoidal inclusions, wound end–to–end around the z axis [21, 22]. The position vector

$$\mathbf{r}(\vartheta, \varphi) = \frac{\eta}{\sqrt{\gamma_\tau \gamma_b}} \underline{\underline{U}} \cdot [\sin \vartheta \cos \varphi \mathbf{u}_n + \cos \vartheta \mathbf{u}_\tau + \sin \vartheta \sin \varphi \mathbf{u}_b], \quad \vartheta \in [0, \pi], \quad \varphi \in [0, 2\pi] \quad (1)$$

prescribes the surface of a particular ellipsoid relative to its centroid. Herein η is a linear measure of size

while the shape dyadic

$$\underline{\underline{U}} = \mathbf{u}_n \mathbf{u}_n + \gamma_\tau \mathbf{u}_\tau \mathbf{u}_\tau + \gamma_b \mathbf{u}_b \mathbf{u}_b \quad (2)$$

is expressed in terms of the normal, tangential, and binormal basis vectors per

$$\left. \begin{aligned} \mathbf{u}_n &= -\mathbf{u}_x \sin \chi + \mathbf{u}_z \cos \chi \\ \mathbf{u}_\tau &= \mathbf{u}_x \cos \chi + \mathbf{u}_z \sin \chi \\ \mathbf{u}_b &= -\mathbf{u}_y \end{aligned} \right\}, \quad (3)$$

with χ denoting the inclination angle relative to the xy plane. An elongated ellipsoidal shape is achieved by selecting the shape parameters $\gamma_b \gtrsim 1$ and $\gamma_\tau \gg 1$. Since increasing γ_τ beyond 10 does not result in significant effects for slim inclusions [22], the value $\gamma_\tau = 15$ is taken for the numerical results presented in §3.

The proportion of a CSTF's total volume occupied by helical nanowires is represented by $f \in (0, 1)$. That is to say, the volume fraction $1 - f$ of a CSTF is not occupied by nanowires.

Let us suppose now that the CSTF under consideration occupies the region $-L \leq z \leq L$, and is unbounded in extent in directions perpendicular to the z axis. At length scales much greater than the nanoscale, the CSTF is characterized by the relative permittivity dyadic

$$\underline{\underline{\epsilon}}_{cstf} = \underline{\underline{S}}_z \left[h \frac{\pi(z+L)}{\Omega} \right] \cdot \underline{\underline{S}}_y(\chi) \cdot \underline{\underline{\epsilon}}_{cstf}^{(\nu)} \cdot \underline{\underline{S}}_y^T(\chi) \cdot \underline{\underline{S}}_z^T \left[h \frac{\pi(z+L)}{\Omega} \right], \quad z \in [-L, L], \quad (4)$$

with the rotation dyadics

$$\left. \begin{aligned} \underline{\underline{S}}_y(\chi) &= \mathbf{u}_y \mathbf{u}_y + (\mathbf{u}_x \mathbf{u}_x + \mathbf{u}_z \mathbf{u}_z) \cos \chi + (\mathbf{u}_z \mathbf{u}_x - \mathbf{u}_x \mathbf{u}_z) \sin \chi \\ \underline{\underline{S}}_z(\sigma) &= \mathbf{u}_z \mathbf{u}_z + (\mathbf{u}_x \mathbf{u}_x + \mathbf{u}_y \mathbf{u}_y) \cos \sigma + (\mathbf{u}_y \mathbf{u}_x - \mathbf{u}_x \mathbf{u}_y) \sin \sigma \end{aligned} \right\}. \quad (5)$$

The structural period is 2Ω , and the handedness parameter $h = +1(-1)$ for a structurally right (left)-handed CSTF. The reference relative permittivity dyadic $\underline{\underline{\epsilon}}_{cstf}^{(\nu)}$ characterizes the local orthorhombic symmetry; i.e.,

$$\underline{\underline{\epsilon}}_{cstf}^{(\nu)} = \epsilon_{a\nu} \mathbf{u}_n \mathbf{u}_n + \epsilon_{b\nu} \mathbf{u}_\tau \mathbf{u}_\tau + \epsilon_{c\nu} \mathbf{u}_b \mathbf{u}_b, \quad (6)$$

with $\nu = 1$ denoting an uninfiltated CSTF (in which case the void regions between nanowires are assumed to be vacuum) and $\nu = 2$ denoting a CSTF in which the void regions are filled with a fluid of refractive index n_ℓ .

We are required to estimate the relative permittivity parameters $\{\epsilon_{a2}, \epsilon_{b2}, \epsilon_{c2}\}$ for an infiltated CSTF from a knowledge of the corresponding parameters $\{\epsilon_{a1}, \epsilon_{b1}, \epsilon_{c1}\}$ for an uninfiltated CSTF. A two-step strategy is employed. The first step is the estimation of the nanoscale parameters $\{n_s, f, \gamma_b\}$ — which are not readily determined by experimental means — from a knowledge of $\{\epsilon_{a1}, \epsilon_{b1}, \epsilon_{c1}\}$. As described in detail elsewhere [17], this can be achieved by applying the inverse Bruggeman homogenization formalism. Once $\{n_s, f, \gamma_b\}$ have been estimated, the second step can be taken wherein these parameters characterizing the uninfiltated CSTF are combined with $\{n_\ell, \gamma_\tau\}$ in order to determine the relative permittivity parameters $\{\epsilon_{a2}, \epsilon_{b2}, \epsilon_{c2}\}$ for the infiltated CSTF, by applying the Bruggeman homogenization formalism in its usual forward sense [8, 22]. For this second step we implement the extended version of the Bruggeman formalism which takes into account the nonzero size of the ellipsoidal inclusion particles [23]. That is, the size parameter η is taken to be small relative to wavelength(s) but nonzero. Details of the extended Bruggeman formalism, applicable to the locally anisotropic dielectric materials under consideration here, is provided in the Appendix.

2.2 Radiation from dipole source inside an infiltated CSTF

2.2.1 Spectral Green function formulation

Let us now introduce an electric dipole of moment $p/2$, oriented in the direction of the unit vector \mathbf{u}_J , which is embedded inside the CSTF at $\mathbf{r} = d \mathbf{u}_z$, $d \in (-L, L)$. The corresponding source current density phasor is

given by

$$\mathbf{J}(\mathbf{r}, \omega) = -\frac{i\omega p}{2} \mathbf{u}_J \delta(z-d) \delta(x) \delta(y), \quad (7)$$

where $\delta(\cdot)$ is the Dirac delta function. With a view to implementing a spectral–Green–function formalism [24], the spatial Fourier transform representation

$$\mathbf{J}(\mathbf{r}, \omega) = \frac{1}{4\pi^2} \int_0^\infty d\kappa \kappa \int_0^{2\pi} d\psi \mathbf{j}(z, \kappa, \psi, \omega) \exp[i\kappa(x \cos \psi + y \sin \psi)] \quad (8)$$

is adopted, with $\mathbf{j}(z, \kappa, \psi, \omega) = -(i\omega p/2) \mathbf{u}_J \delta(z-d)$ in accordance with eq. (7).

Our attention is focused on a single spatial–Fourier component of $\mathbf{J}(\mathbf{r}, \omega)$, i.e.,

$$\mathbf{J}(\mathbf{r}, \kappa, \psi, \omega) = \mathbf{j}(z, \kappa, \psi, \omega) \exp[i\kappa(x \cos \psi + y \sin \psi)], \quad z \in (-L, L). \quad (9)$$

Similarly, we write the electromagnetic field phasors inside the CSTF as

$$\left. \begin{aligned} \mathbf{E}(\mathbf{r}, \kappa, \psi, \omega) &= \mathbf{e}(z, \kappa, \psi, \omega) \exp[i\kappa(x \cos \psi + y \sin \psi)], \\ \mathbf{H}(\mathbf{r}, \kappa, \psi, \omega) &= \mathbf{h}(z, \kappa, \psi, \omega) \exp[i\kappa(x \cos \psi + y \sin \psi)] \end{aligned} \right\}, \quad z \in (-L, L). \quad (10)$$

The procedure whereby the Fourier components (9) and (10) are combined with the constitutive relations for the CSTF and the frequency–domain Maxwell curl postulates, and then solved to find expressions for the phasors inside the CSTF, is comprehensively described elsewhere [16]. Therefore, here we simply state the particular solution

$$\begin{aligned} [\mathbf{f}(L, \kappa, \psi, \omega)] &= [\mathbf{M}(L, \kappa, \psi, \omega)] [\mathbf{f}(-L, \kappa, \psi, \omega)] \\ &\quad - i\omega \frac{p}{2} [\mathbf{M}(L, \kappa, \psi, \omega)] [\mathbf{M}(d, \kappa, \psi, \omega)]^{-1} [\tilde{\mathbf{g}}(d, \kappa, \psi, \omega)], \end{aligned} \quad (11)$$

wherein the column vectors

$$[\mathbf{f}(z, \kappa, \psi, \omega)] = \begin{bmatrix} \mathbf{e}(z, \kappa, \psi, \omega) \cdot \mathbf{u}_x \\ \mathbf{e}(z, \kappa, \psi, \omega) \cdot \mathbf{u}_y \\ \mathbf{h}(z, \kappa, \psi, \omega) \cdot \mathbf{u}_x \\ \mathbf{h}(z, \kappa, \psi, \omega) \cdot \mathbf{u}_y \end{bmatrix} \quad (12)$$

and

$$[\tilde{\mathbf{g}}(z, \kappa, \psi, \omega)] = \frac{\mathbf{u}_J \cdot \mathbf{u}_z}{\epsilon_{a\nu} \cos^2 \chi + \epsilon_{b\nu} \sin^2 \chi} \begin{bmatrix} \frac{\kappa \cos \psi}{\omega \epsilon_0} \\ \frac{\kappa \sin \psi}{\omega \epsilon_0} \\ (\epsilon_{a\nu} - \epsilon_{b\nu}) \sin \chi \cos \chi \sin \left[h \frac{\pi(z+L)}{\Omega} \right] \\ (\epsilon_{b\nu} - \epsilon_{a\nu}) \sin \chi \cos \chi \cos \left[h \frac{\pi(z+L)}{\Omega} \right] \end{bmatrix} + \begin{bmatrix} 0 \\ 0 \\ \mathbf{u}_J \cdot \mathbf{u}_y \\ -\mathbf{u}_J \cdot \mathbf{u}_x \end{bmatrix}. \quad (13)$$

The expressions for the 4×4 matrizants $[\mathbf{M}(L, \kappa, \psi, \omega)]$ and $[\mathbf{M}(d, \kappa, \psi, \omega)]$ — which are straightforwardly derived, but too cumbersome to reproduce here — are available in standard works [1, Chap. 9]. We note that the piecewise uniform approximation technique provides a convenient method for their evaluation [1, Chap. 9].

2.2.2 Boundary value problem

Next we turn to the two half–spaces $z < -L$ and $z > L$. The half–space $z < -L$ is vacuous while the half–space $z > L$ is filled by a fluid of refractive index n_ℓ . In consonance with eqs. (10), the electromagnetic field phasors for these two half–spaces may be expressed as

$$\left. \begin{aligned} \mathbf{E}(\mathbf{r}, \kappa, \psi, \omega) &= \frac{1}{\sqrt{2}} [-b_L(\kappa, \psi, \omega) (i\mathbf{s} - \mathbf{p}_-) + b_R(\kappa, \psi, \omega) (i\mathbf{s} + \mathbf{p}_-)] \\ &\quad \times \exp\{i[\kappa(x \cos \psi + y \sin \psi) - \alpha_0(z+L)]\} \\ \mathbf{H}(\mathbf{r}, \kappa, \psi, \omega) &= \frac{i}{\eta_0 \sqrt{2}} [b_L(\kappa, \psi, \omega) (i\mathbf{s} - \mathbf{p}_-) + b_R(\kappa, \psi, \omega) (i\mathbf{s} + \mathbf{p}_-)] \\ &\quad \times \exp\{i[\kappa(x \cos \psi + y \sin \psi) - \alpha_0(z+L)]\} \end{aligned} \right\}, \quad z < -L, \quad (14)$$

and

$$\left. \begin{aligned} \mathbf{E}(\mathbf{r}, \kappa, \psi, \omega) &= \frac{1}{\sqrt{2}} [c_L(\kappa, \psi, \omega) (i\mathbf{s} - \mathbf{p}_+) - c_R(\kappa, \psi, \omega) (i\mathbf{s} + \mathbf{p}_+)] \\ &\quad \times \exp \{i [\kappa (x \cos \psi + y \sin \psi) + \alpha_\ell (z - L)]\} \\ \mathbf{H}(\mathbf{r}, \kappa, \psi, \omega) &= -\frac{i}{\eta_\ell \sqrt{2}} [c_L(\kappa, \psi, \omega) (i\mathbf{s} - \mathbf{p}_+) + c_R(\kappa, \psi, \omega) (i\mathbf{s} + \mathbf{p}_+)] \\ &\quad \times \exp \{i [\kappa (x \cos \psi + y \sin \psi) + \alpha_\ell (z - L)]\} \end{aligned} \right\}, \quad z > L, \quad (15)$$

where $\alpha_0 = +\sqrt{k_0^2 - \kappa^2}$, $\alpha_\ell = +\sqrt{k_\ell^2 - \kappa^2}$, $k_\ell = k_0 n_\ell$ and $\eta_\ell = \eta_0/n_\ell$. The complex-valued amplitudes $b_L(\kappa, \psi, \omega)$ and $c_L(\kappa, \psi, \omega)$ represent the LCP components, while $b_R(\kappa, \psi, \omega)$ and $c_R(\kappa, \psi, \omega)$ likewise represent the RCP components. The unit vectors

$$\mathbf{s} = -\mathbf{u}_x \sin \psi + \mathbf{u}_y \cos \psi \quad (16)$$

and

$$\mathbf{p}_\pm = \begin{cases} \mp(\alpha_0/k_0) (\mathbf{u}_x \cos \psi + \mathbf{u}_y \sin \psi) + (\kappa/k_0) \mathbf{u}_z, & z < -L \\ \mp(\alpha_\ell/k_\ell) (\mathbf{u}_x \cos \psi + \mathbf{u}_y \sin \psi) + (\kappa/k_\ell) \mathbf{u}_z, & z > L \end{cases} \quad (17)$$

relate to the perpendicular- and parallel-polarization states of the plane wave, respectively.

The tangential components of $\mathbf{E}(\mathbf{r}, \kappa, \psi, \omega)$ and $\mathbf{H}(\mathbf{r}, \kappa, \psi, \omega)$ are required to be continuous across the pupils at $z = -L$ and $z = L$ of the CSTF. Thus we have that

$$[\mathbf{f}(-L, \kappa, \psi, \omega)] = \frac{1}{\sqrt{2}} [\mathbf{K}(\kappa, \psi, \omega, \alpha_0, k_0, \eta_0)] \begin{bmatrix} 0 \\ 0 \\ -i [b_L(\kappa, \psi, \omega) - b_R(\kappa, \psi, \omega)] \\ b_L(\kappa, \psi, \omega) + b_R(\kappa, \psi, \omega) \end{bmatrix} \quad (18)$$

and

$$[\mathbf{f}(L, \kappa, \psi, \omega)] = \frac{1}{\sqrt{2}} [\mathbf{K}(\kappa, \psi, \omega, \alpha_\ell, k_\ell, \eta_\ell)] \begin{bmatrix} i [c_L(\kappa, \psi, \omega) - c_R(\kappa, \psi, \omega)] \\ - [c_L(\kappa, \psi, \omega) + c_R(\kappa, \psi, \omega)] \\ 0 \\ 0 \end{bmatrix} \quad (19)$$

where

$$[\mathbf{K}(\kappa, \psi, \omega, \alpha, k, \eta)] = \begin{bmatrix} -\sin \psi & -\frac{\alpha \cos \psi}{k} & -\sin \psi & \frac{\alpha \cos \psi}{k} \\ \cos \psi & -\frac{\alpha \sin \psi}{k} & \cos \psi & \frac{\alpha \sin \psi}{k} \\ -\frac{\alpha \cos \psi}{k\eta} & \frac{\sin \psi}{\eta} & \frac{\alpha \cos \psi}{k\eta} & \frac{\sin \psi}{\eta} \\ -\frac{\alpha \sin \psi}{k\eta} & -\frac{\cos \psi}{\eta} & \frac{\alpha \sin \psi}{k\eta} & -\frac{\cos \psi}{\eta} \end{bmatrix}. \quad (20)$$

The unknown four amplitudes $b_{L,R}(\kappa, \psi, \omega)$ and $c_{L,R}(\kappa, \psi, \omega)$ can now be determined using standard algebraic manipulations, by combining eqs. (18) and (19) with the particular solution (11).

2.2.3 Emitted far-field phasors

The emitted electromagnetic phasors in the half-spaces $z < -L$ and $z > L$ are found by summing the corresponding spatial Fourier components (14) and (15) per

$$\left. \begin{aligned} \mathbf{E}(\mathbf{r}, \omega) &= \frac{1}{4\pi^2} \int_0^\infty d\kappa \int_0^{2\pi} d\psi \kappa \mathbf{E}(\mathbf{r}, \kappa, \psi, \omega) \\ \mathbf{H}(\mathbf{r}, \omega) &= \frac{1}{4\pi^2} \int_0^\infty d\kappa \int_0^{2\pi} d\psi \kappa \mathbf{H}(\mathbf{r}, \kappa, \psi, \omega) \end{aligned} \right\}, \quad z \notin [-L, L]. \quad (21)$$

Asymptotic approximations to these integrals, representing the emitted field phasors in the far zone, are provided by [25, 26]

$$\left. \begin{aligned} \mathbf{E}(\mathbf{r}^{obs}, \omega) &\approx \frac{i \cos \theta^{obs}}{2\sqrt{2}\pi} [-b_L^{obs} (i\mathbf{s}^{obs} - \mathbf{p}_-^{obs}) + b_R^{obs} (i\mathbf{s}^{obs} + \mathbf{p}_-^{obs})] \frac{\exp(ik_0 \tilde{r}_-^{obs})}{k_0 \tilde{r}_-^{obs}} \\ \mathbf{H}(\mathbf{r}^{obs}, \omega) &\approx -\frac{\cos \theta^{obs}}{\eta_0 2\sqrt{2}\pi} [b_L^{obs} (i\mathbf{s}^{obs} - \mathbf{p}_-^{obs}) + b_R^{obs} (i\mathbf{s}^{obs} + \mathbf{p}_-^{obs})] \frac{\exp(ik_0 \tilde{r}_-^{obs})}{k_0 \tilde{r}_-^{obs}} \end{aligned} \right\}, \quad z^{obs} < -L \quad (22)$$

and

$$\left. \begin{aligned} \mathbf{E}(\mathbf{r}^{obs}, \omega) &\approx \frac{i \cos \theta^{obs}}{2\sqrt{2}\pi} [c_L^{obs} (i\mathbf{s}^{obs} - \mathbf{p}_+^{obs}) - c_R^{obs} (i\mathbf{s}^{obs} + \mathbf{p}_+^{obs})] \frac{\exp(ik_\ell \tilde{r}_+^{obs})}{k_\ell \tilde{r}_+^{obs}} \\ \mathbf{H}(\mathbf{r}^{obs}, \omega) &\approx \frac{\cos \theta^{obs}}{\eta_\ell 2\sqrt{2}\pi} [c_L^{obs} (i\mathbf{s}^{obs} - \mathbf{p}_+^{obs}) + c_R^{obs} (i\mathbf{s}^{obs} + \mathbf{p}_+^{obs})] \frac{\exp(ik_\ell \tilde{r}_+^{obs})}{k_\ell \tilde{r}_+^{obs}} \end{aligned} \right\}, \quad z^{obs} > L, \quad (23)$$

wherein $\tilde{r}_\pm^{obs} = |\mathbf{r}^{obs} \mp L\mathbf{u}_z|$ and the superscript *obs* denotes evaluation at the distant observation point $\mathbf{r}^{obs} \equiv (r^{obs}, \theta^{obs}, \psi^{obs})$ with $z^{obs} = \mathbf{r}^{obs} \cdot \mathbf{u}_z$. Note that the approximations (22) and (23) are appropriate at distances far from the CSTF pupils but not in the vicinity of $\theta^{obs} = \pi/2$ [25, 26].

For practical purposes, the radiation field in the far zone is conveniently characterized in terms of the time-averaged Poynting vector, which we write as the sum of LCP and RCP contributions per

$$\mathbf{P}(\mathbf{r}^{obs}, \omega) = \mathbf{P}_{LCP}(\mathbf{r}^{obs}, \omega) + \mathbf{P}_{RCP}(\mathbf{r}^{obs}, \omega), \quad (24)$$

wherein

$$\mathbf{P}_{LCP}(\mathbf{r}^{obs}, \omega) \approx \begin{cases} \frac{1}{2\eta_0} (|b_L^{obs}|^2) \left(\frac{\cos \theta^{obs}}{2\pi k_0 \tilde{r}_-^{obs}} \right)^2 \hat{\mathbf{r}}^{obs}, & z^{obs} < -L \\ \frac{1}{2\eta_\ell} (|c_L^{obs}|^2) \left(\frac{\cos \theta^{obs}}{2\pi k_\ell \tilde{r}_+^{obs}} \right)^2 \hat{\mathbf{r}}^{obs}, & z^{obs} > L \end{cases} \quad (25)$$

and

$$\mathbf{P}_{RCP}(\mathbf{r}^{obs}, \omega) \approx \begin{cases} \frac{1}{2\eta_0} (|b_R^{obs}|^2) \left(\frac{\cos \theta^{obs}}{2\pi k_0 \tilde{r}_-^{obs}} \right)^2 \hat{\mathbf{r}}^{obs}, & z^{obs} < -L \\ \frac{1}{2\eta_\ell} (|c_R^{obs}|^2) \left(\frac{\cos \theta^{obs}}{2\pi k_\ell \tilde{r}_+^{obs}} \right)^2 \hat{\mathbf{r}}^{obs}, & z^{obs} > L \end{cases} \quad (26)$$

at the observation point $\mathbf{r}^{obs} = r^{obs} \hat{\mathbf{r}}^{obs}$.

3 Numerical results

For our numerical investigations we selected a structurally right-handed CSTF (i.e., $h = +1$) with structural half-period $\Omega = 200$ nm. Experimentally-determined values for the relative permittivity parameters $\{\epsilon_{a1}, \epsilon_{b1}, \epsilon_{c1}\}$, which characterize the unfiltered scenario, were used. In light of the absence of appropriate data for CSTFs, we chose the relative permittivity parameters

$$\left. \begin{aligned} \epsilon_{a1} &= \left[1.0443 + 2.7394 \left(\frac{2\chi_v}{\pi} \right) - 1.3697 \left(\frac{2\chi_v}{\pi} \right)^2 \right]^2 \\ \epsilon_{b1} &= \left[1.6765 + 1.5649 \left(\frac{2\chi_v}{\pi} \right) - 0.7825 \left(\frac{2\chi_v}{\pi} \right)^2 \right]^2 \\ \epsilon_{c1} &= \left[1.3586 + 2.1109 \left(\frac{2\chi_v}{\pi} \right) - 1.0554 \left(\frac{2\chi_v}{\pi} \right)^2 \right]^2 \end{aligned} \right\} \quad (27)$$

with

$$\tan \chi = 2.8818 \tan \chi_v, \quad (28)$$

which were determined by measurements on a columnar thin film made from patinal[®] titanium oxide [27, 28]. The angle χ_v (radians) in eqs. (27) represents the average direction of the vapour flux relative to the substrate during the deposition process. As described in a previous study [17], the inverse Bruggeman homogenization formalism yields the corresponding nanoscale model parameter values: $n_s = 3.0517$, $f = 0.5039$ and $\gamma_b = 1.8381$ for the vapour flux angle $\chi_v = 30^\circ$.

The relative permittivity parameters $\{\epsilon_{a2}, \epsilon_{b2}, \epsilon_{c2}\}$ for the infiltrated CSTF, as computed using the extended Bruggeman homogenization formalism, are graphed as functions of the refractive index of the infiltrating fluid $n_\ell \in (1.0, 1.5)$ and the relative size parameter $k_0\eta \in (0, 0.2)$ in Fig. 2. The real parts of $\{\epsilon_{a2}, \epsilon_{b2}, \epsilon_{c2}\}$ increase uniformly as n_ℓ increases; they also increase uniformly as η increases but more slowly. The imaginary parts of $\{\epsilon_{a2}, \epsilon_{b2}, \epsilon_{c2}\}$ are fairly insensitive to n_ℓ , but these quantities increase exponentially as the size parameter increases from zero. The manifestation of constitutive parameters with nonzero imaginary parts for homogenized composite materials, when the component materials are themselves nondissipative, is a well-recognized phenomenon. This phenomenon — which arises in higher-order homogenization theories, such as the strong-property-fluctuation theory [29, 30] and extended variants of the Bruggeman and Maxwell Garnett formalisms [31, 32, 33] — may be attributed to radiative scattering loss from the macroscopic coherent field [34]. In particular, we note that $\text{Im} \epsilon_{a2, b2, c2} \rightarrow 0$ in the limit as $\eta \rightarrow 0$.

Now let us turn to the radiation emitted from a dipole source embedded within the CSTF. We chose the source to be located relatively close to the upper surface of the CSTF at $d = L - 40$ nm; and the source orientation was given by $\mathbf{u}_J = \underline{\underline{z}}_z(d, h) \cdot \mathbf{u}_n^2$. From the point of view of sensor applications, we are particularly interested in the ability of the CSTF to discriminate between LCP and RCP light. Accordingly, the wavelength ranges considered here were selected to include the circular Bragg regime. The location and extent of the the circular Bragg regime were conveniently estimated by the centre wavelength [1]

$$\lambda_0^{Br}(\epsilon_{av}, \epsilon_{bv}, \epsilon_{cv}, \theta^{obs}) \simeq \Omega \left(\sqrt{|\epsilon_{cv}|} + \sqrt{\left| \frac{\epsilon_{av}\epsilon_{bv}}{\epsilon_{av} \cos^2 \chi + \epsilon_{av} \sin^2 \chi} \right|} \right) \sqrt{\cos \theta^{obs}}, \quad (29)$$

and the full-width-at-half-maximum bandwidth [1]

$$(\Delta\lambda_0)^{Br}(\epsilon_{av}, \epsilon_{bv}, \epsilon_{cv}, \theta^{obs}) \simeq 2\Omega \left(\sqrt{|\epsilon_{cv}|} - \sqrt{\left| \frac{\epsilon_{av}\epsilon_{bv}}{\epsilon_{av} \cos^2 \chi + \epsilon_{av} \sin^2 \chi} \right|} \right) \sqrt{\cos \theta^{obs}}. \quad (30)$$

The thickness ratio $L/\Omega = 30$ was chosen to ensure that the circular Bragg phenomenon is fully developed.

In order to appreciate the effects of infiltration, we must first consider the uninfiltrated scenario. In Fig. 3, the projections of $|\mathbf{P}_{LCP}(\mathbf{r}^{obs}, \omega)|$ and $|\mathbf{P}_{RCP}(\mathbf{r}^{obs}, \omega)|$ onto the $z = 0$ plane are mapped for $n_\ell = 1$ (i.e., $\nu = 1$). The contributions to the time-averaged Poynting vector were scaled by a factor of $10^{13}\omega^{-2}|p|^{-2}$. The radiation emitted through the CSTF's pupils at $z = L$ and $z = -L$ are both represented. Results are presented for $\lambda_0 = \lambda_0^{Br}(\epsilon_{a1}, \epsilon_{b1}, \epsilon_{c1}, 0^\circ) = 763.6$ nm, as well as for $\lambda_0 = \lambda_0^{Br}(\epsilon_{a1}, \epsilon_{b1}, \epsilon_{c1}, 0^\circ) - 80$ nm and $\lambda_0 = \lambda_0^{Br}(\epsilon_{a1}, \epsilon_{b1}, \epsilon_{c1}, 0^\circ) + 40$ nm. Also presented in Fig. 3 are evaluations of the real-valued parameter

$$\Gamma_j = \frac{10^{16}}{\omega^2 |p|^2} \int_{\theta^{obs}=\rho_1}^{\rho_2} d\theta^{obs} \int_{\psi^{obs}=0}^{2\pi} d\psi^{obs} (r^{obs})^2 \sin \theta^{obs} |\mathbf{P}_j(\mathbf{r}^{obs}, \omega)|, \quad j \in \{LCP, RCP\}, \quad (31)$$

wherein $\rho_1 = 0$, $\rho_2 = 0.95\pi/2$ for $z^{obs} > L$, and $\rho_1 = \pi - (0.95\pi/2)$, $\rho_2 = \pi$ for $z^{obs} < -L$. The quantity Γ_j delivers a measure of the total rate of energy flow into the half-spaces $z > L$ and $z < -L$.

There are several notable features in Fig. 3, especially concerning differences between the LCP and RCP emission characteristics, which relate to the circular Bragg phenomenon: (i) For emission which is

²We also considered the source orientations $\mathbf{u}_J = \underline{\underline{z}}_z(d, h) \cdot \mathbf{u}_\tau$ and $\mathbf{u}_J = \underline{\underline{z}}_z(d, h) \cdot \mathbf{u}_b$. The results for these cases are not presented here as they were qualitatively similar to the case $\mathbf{u}_J = \underline{\underline{z}}_z(d, h) \cdot \mathbf{u}_n$.

approximately normal to the two pupils of the CSTF, RCP radiation is preferentially emitted through the pupil at $z = L$ for $\lambda_0 = 763.6$ nm whereas at the same wavelength LCP radiation is preferentially emitted through the pupil at $z = -L$. (ii) At $\lambda_0 = 683.6$ nm, the differences between LCP and RCP emission are very small for $|\cos\theta^{obs}| \simeq 1$, but we can see that RCP radiation is preferentially emitted through the upper pupil whereas LCP radiation is preferentially emitted through the lower pupil for $0.4 \lesssim |\cos\theta^{obs}| \lesssim 0.8$. This observation is in accordance with the blue shift of the circular Bragg phenomenon for obliquely incident plane waves [1]. (iii) The distinction between the LCP and RCP patterns is barely noticeable when $|\cos\theta^{obs}| \lesssim 0.4$, for all three wavelengths considered. This is indicative of the severe diminishment of the circular Bragg phenomenon for highly oblique planewave incidence [35]. (iv) There is very little evidence of the CSTF discriminating between LCP and RCP radiation at $\lambda_0 = 803.6$ nm; this wavelength represents an upper bound on the circular Bragg phenomenon for all angles of incidence.

Let us remark too upon the distinctive pattern of concentric rings that appears in Fig. 3. These are Fabry–Perot interference rings, arising due to the finite thickness of the CSTF. Indeed, even if the CSTF were replaced by a homogeneous isotropic dielectric material the ring pattern would still be observed [16].

The results of infiltration can be observed in Figs. 4 and 5, which show the projections of $|\mathbf{P}_{LCP}(\mathbf{r}^{obs}, \omega)|$ and $|\mathbf{P}_{RCP}(\mathbf{r}^{obs}, \omega)|$ (as before, scaled by a factor of $10^{13}\omega^{-2}|p|^{-2}$) onto the $z = 0$ plane for $n_\ell = 1.25$ and $n_\ell = 1.5$, respectively. The relative permittivity parameters $\{\epsilon_{a2}, \epsilon_{b2}, \epsilon_{c2}\}$ for the infiltrated CSTF were computed using the non-extended version of the Bruggeman homogenization formalism (or, equivalently, the extended version with $\eta = 0$). In keeping with Fig. 3, results are presented for $\lambda_0 = \lambda_0^{Br}(\epsilon_{a2}, \epsilon_{b2}, \epsilon_{c2}, 0^\circ)$, as well as for $\lambda_0 = \lambda_0^{Br}(\epsilon_{a2}, \epsilon_{b2}, \epsilon_{c2}, 0^\circ) - 80$ nm and $\lambda_0 = \lambda_0^{Br}(\epsilon_{a2}, \epsilon_{b2}, \epsilon_{c2}, 0^\circ) + 40$ nm. As for the unfiltered case, we see that RCP radiation is preferentially emitted through the pupil at $z = L$ whereas LCP radiation is preferentially emitted through the pupil at $z = -L$, at the centre Bragg wavelength $\lambda_0^{Br}(\epsilon_{a2}, \epsilon_{b2}, \epsilon_{c2}, \theta^{obs})$ for $|\cos\theta^{obs}| \simeq 1$. Two effects in particular of infiltration are apparent from Figs. 4 and 5 as the refractive index of the infiltrating fluid increases: (i) the distinction between LCP/RCP emission for $|\cos\theta^{obs}| \simeq 1$ becomes increasingly red shifted; and (ii) the blue shift in the distinction between LCP/RCP emission for oblique angles of incidence becomes less pronounced.

In fact, the main effects of infiltration are quite well predicted via the empirical relations (29) and (30). To see this, the centre Bragg wavelength and the full-width-at-half-maximum bandwidth are plotted versus n_ℓ in Fig. 6. As in Figs. 4 and 5, the non-extended version of the Bruggeman homogenization formalism was used to estimate the relative permittivity parameters $\{\epsilon_{a2}, \epsilon_{b2}, \epsilon_{c2}\}$. The red shift in the centre wavelength, and the reduction in the full-width-at-half-maximum bandwidth, resulting from the refractive index of the infiltrating fluid being increased are obvious from Fig. 6 — and these effects are in complete agreement with the emission patterns observed in Figs. 3–5.

We consider now the influence of the linear size of the ellipsoidal particles which represent the CSTF’s helical nanowires, per the homogenization model described in §2.1. As a representative example, we repeat the calculations of Fig. 4 but here using the extended Bruggeman homogenization formalism to estimate the relative permittivity parameters $\{\epsilon_{a2}, \epsilon_{b2}, \epsilon_{c2}\}$ of the infiltrated CSTF. We set the size parameter to be $\eta = 0.1/k_0$. The corresponding projections of $|\mathbf{P}_{LCP}(\mathbf{r}^{obs}, \omega)|$ and $|\mathbf{P}_{RCP}(\mathbf{r}^{obs}, \omega)|$ (as before, scaled by a factor of $10^{13}\omega^{-2}|p|^{-2}$) onto the $z = 0$ plane are provided in Fig. 7 for $n_\ell = 1.25$. By comparing Figs. 4 and 7, we see that the size parameter has a relatively minor but significant influence on the emission patterns. The centre wavelength for the distinction between LCP/RCP emission is slightly higher in Fig. 7 as compared to Fig. 4. Furthermore, the total energy flux emitted from the CSTF — as estimated by the scalar parameter $\Gamma_{LCP,RCP}$ — is substantially smaller when we consider $\eta = 0.1/k_0$ as opposed to $\eta = 0$. This is most noticeable for radiation emitted through the CSTF pupil at $z = -L$, which is a consequence of the dipole source being closer to the $z = L$ pupil.

The main effects of the size parameter η may be estimated quite well using the empirical relations (29) and (30). In Fig. 8, $\lambda_0^{Br}(\epsilon_{a2}, \epsilon_{b2}, \epsilon_{c2}, 0^\circ)$ and $\Delta\lambda_0^{Br}(\epsilon_{a2}, \epsilon_{b2}, \epsilon_{c2}, 0^\circ)$ are plotted versus $k_0\eta$ for $n_\ell \in \{1.0, 1.25, 1.5\}$. The modest increase in the centre Bragg wavelength is clear; and we note that the rate of increase is greatest when the refractive index of the infiltrating fluid is smallest. The full-width-at-half-maximum bandwidth is relatively insensitive to the size parameter η , regardless of the value of n_ℓ . Qualitatively similar results are found when angles $\theta^{obs} > 0^\circ$ are considered.

4 Closing remarks

Using a spectral Green function formalism, in conjunction with an inverse homogenization formalism, the effect of infiltration on the emission from a dipole source embedded within a CSTF has been characterized. Based on numerical studies, our conclusions may be summarized as:

- The centre wavelength for the preferential emission of LCP/RCP radiation is red shifted as the refractive index of the infiltrating fluid increases from unity. Furthermore, the red shift is accentuated when the size of the ellipsoidal particles which represent the helical nanowires of the CSTF is increased.
- The bandwidth of the preferential LCP/RCP emission regime decreases as the refractive index of the infiltrating fluid increases from unity.
- The main effects of infiltration may be reasonably predicted using the simple empirical formulas (29) and (30) which provide estimates of the centre Bragg wavelength and the corresponding full-width-at-half-maximum bandwidth.

Through the elucidation of the effects of infiltration, a further step towards the practical realization of CSTF-based optical sensors, including biosensors which harness chemiluminescent emission from inside a CSTF, has been taken.

Acknowledgements

SSJ is supported by Universiti Tun Hussein Onn Malaysia. During part of this study TGM was supported by a Royal Academy of Engineering/Leverhulme Trust Senior Research Fellowship.

Appendix

In order to estimate the reference relative permittivity dyadic of an infiltrated CSTF, a local homogenization procedure is carried out within a plane parallel to $z = 0$. Two components are to be homogenized: (i) a planar array of similarly-aligned ellipsoidal particles — of refractive index n_s and specified by the linear size parameter η and shape dyadic $\underline{\underline{U}}$ per eq. (1) — which are the building blocks of the helical nanowires; and (ii) void regions — represented as a collection of spherical particles, of radius specified the linear size parameter η — which are infiltrated with a fluid of refractive index n_ℓ . The linear size parameter η is taken to be much smaller than the wavelength(s) but not vanishingly small.

From the nonlinear Bruggeman equation [23]

$$(1 - f) \underline{\underline{\alpha}}_{\ell/(2)} + f \underline{\underline{\alpha}}_{s/(2)} = \underline{\underline{0}}, \quad (32)$$

$\underline{\underline{\epsilon}}_{cstf}^{(2)}$ can be extracted by standard numerical methods, such as the Jacobi technique [36]. Herein, the polarizability density dyadics

$$\left. \begin{aligned} \underline{\underline{\alpha}}_{\ell/(2)} &= \left(\sqrt{n_\ell} \underline{\underline{I}} - \underline{\underline{\epsilon}}_{cstf}^{(2)} \right) \cdot \left[\underline{\underline{I}} + i\omega \underline{\underline{D}}_{(2)}(\underline{\underline{A}}_\ell) \cdot \left(\sqrt{n_\ell} \underline{\underline{I}} - \underline{\underline{\epsilon}}_{cstf}^{(2)} \right) \right]^{-1} \\ \underline{\underline{\alpha}}_{s/(2)} &= \left(\sqrt{n_s} \underline{\underline{I}} - \underline{\underline{\epsilon}}_{cstf}^{(2)} \right) \cdot \left[\underline{\underline{I}} + i\omega \underline{\underline{D}}_{(2)}(\underline{\underline{A}}_s) \cdot \left(\sqrt{n_s} \underline{\underline{I}} - \underline{\underline{\epsilon}}_{cstf}^{(2)} \right) \right]^{-1} \end{aligned} \right\}, \quad (33)$$

where the depolarization dyadics

$$\underline{\underline{D}}_{(2)}(\underline{\underline{A}}) = \frac{1}{4\pi i\omega} \int_0^{2\pi} d\varphi \int_0^\pi d\theta \sin\theta \left(\underline{\underline{W}}^0 + \eta^2 \underline{\underline{W}}^+ \right) \quad (34)$$

with

$$\left. \begin{aligned} \underline{\underline{A}}_s &= \sin^2 \vartheta \cos^2 \varphi \mathbf{u}_n \mathbf{u}_n + \frac{\cos^2 \vartheta}{\gamma_\tau^2} \mathbf{u}_\tau \mathbf{u}_\tau + \frac{\sin^2 \vartheta \sin^2 \varphi}{\gamma_b^2} \mathbf{u}_b \mathbf{u}_b \\ \underline{\underline{A}}_\ell &= \sin^2 \vartheta \cos^2 \varphi \mathbf{u}_n \mathbf{u}_n + \cos^2 \vartheta \mathbf{u}_\tau \mathbf{u}_\tau + \sin^2 \vartheta \sin^2 \varphi \mathbf{u}_b \mathbf{u}_b \end{aligned} \right\}. \quad (35)$$

The dyadic integrands in eq. (34) are given as

$$\underline{\underline{W}}^0 = \frac{1}{\text{tr} \left(\underline{\underline{\epsilon}}_{cstf}^{(2)} \cdot \underline{\underline{A}} \right)} \underline{\underline{A}} \quad (36)$$

and

$$\underline{\underline{W}}^+ = \frac{1}{3\tau} \left\{ \left[\frac{3(\kappa_+ - \kappa_-)}{2} + i\eta \left(\kappa_+^{\frac{3}{2}} - \kappa_-^{\frac{3}{2}} \right) \right] \underline{\underline{a}} + i\eta k_0^2 \left(\kappa_+^{\frac{1}{2}} - \kappa_-^{\frac{1}{2}} \right) \underline{\underline{b}} \right\}, \quad (37)$$

with the 3×3 dyadics

$$\begin{aligned} \underline{\underline{a}} &= \left[2 \underline{\underline{\epsilon}}_{cstf}^{(2)} - \text{tr} \left(\underline{\underline{\epsilon}}_{cstf}^{(2)} \right) \underline{\underline{I}} \right] \cdot \underline{\underline{A}} - \text{tr} \left(\underline{\underline{\epsilon}}_{cstf}^{(2)} \cdot \underline{\underline{A}} \right) \underline{\underline{I}} \\ &\quad - \frac{\text{tr} \left[\left(\underline{\underline{\epsilon}}_{cstf}^{(2)} \right)^{adj} \cdot \underline{\underline{A}} \right] - \left\{ \text{tr} \left[\left(\underline{\underline{\epsilon}}_{cstf}^{(2)} \right)^{adj} \right] \text{tr} \left(\underline{\underline{A}} \right) \right\}}{\text{tr} \left(\underline{\underline{\epsilon}}_{cstf}^{(2)} \cdot \underline{\underline{A}} \right)} \underline{\underline{A}}, \end{aligned} \quad (38)$$

$$\underline{\underline{b}} = \left(\underline{\underline{\epsilon}}_{cstf}^{(2)} \right)^{adj} - \frac{\det \left(\underline{\underline{\epsilon}}_{cstf}^{(2)} \right)}{\text{tr} \left(\underline{\underline{\epsilon}}_{cstf}^{(2)} \cdot \underline{\underline{A}} \right)} \underline{\underline{A}} \quad (39)$$

and scalar quantities

$$\tau = \left(\left\{ \text{tr} \left[\left(\underline{\underline{\epsilon}}_{cstf}^{(2)} \right)^{adj} \cdot \underline{\underline{A}} \right] - \text{tr} \left[\left(\underline{\underline{\epsilon}}_{cstf}^{(2)} \right)^{adj} \right] \text{tr} \left(\underline{\underline{A}} \right) \right\}^2 - 4 \det \left(\underline{\underline{\epsilon}}_{cstf}^{(2)} \right) \text{tr} \left(\underline{\underline{A}} \right) \text{tr} \left(\underline{\underline{\epsilon}}_{cstf}^{(2)} \cdot \underline{\underline{A}} \right) \right)^{\frac{1}{2}}, \quad (40)$$

$$\kappa_\pm = k_0^2 \frac{\left\{ \text{tr} \left[\left(\underline{\underline{\epsilon}}_{cstf}^{(2)} \right)^{adj} \right] \text{tr} \left(\underline{\underline{A}} \right) \right\} - \text{tr} \left[\left(\underline{\underline{\epsilon}}_{cstf}^{(2)} \right)^{adj} \cdot \underline{\underline{A}} \right] \pm \tau}{2 \text{tr} \left(\underline{\underline{A}} \right) \text{tr} \left(\underline{\underline{\epsilon}}_{cstf}^{(2)} \cdot \underline{\underline{A}} \right)}. \quad (41)$$

Numerical methods are generally needed to evaluate the surface integral on the right side of eq. (34) [37].

References

- [1] A. Lakhtakia, R. Messier, *Sculptured Thin Films: Nanoengineered Morphology and Optics*, SPIE Press, Bellingham, WA, USA, 2005.
- [2] I. Hodgkinson, Q. h. Wu, *Adv. Mater.* 13 (2001) 889.
- [3] R. Messier, V. C. Venugopal, P. D. Sunal, *J. Vac. Sci. Technol. A* 18 (2000) 1538.
- [4] J. A. Polo Jr., in: N. P. Mahalik (Ed.), *Micromanufacturing and Nanotechnology*, Springer, Heidelberg, Germany, 2005.
- [5] A. Lakhtakia, M. C. Demirel, M. W. Horn, J. Xu, *Adv. Solid State Phys.* 46 (2007) 295.

- [6] M.-S. Wong, M.-F. Lee, C.-L. Chen, C.-H. Huang, *Thin Solid Films* (2010) doi:10.1016/j.tsf.2010.06.047.
- [7] P. G. de Gennes, J. Prost, *The Physics of Liquid Crystals*, Oxford University Press, New York, NY, USA, 1993.
- [8] T.G. Mackay, A. Lakhtakia, *IEEE Photonics J.* 2 (2010) 92.
- [9] T.G. Mackay and A. Lakhtakia, *IEEE Sensors J.* (2010) doi:10.1109/JSEN.2010.2067448.
- [10] A. Lakhtakia, *Opt. Commun.* 188 (2001) 313.
- [11] A. Fan, Z. Cao, H. Li, M. Kai, J. Lu, *Analytical Sciences* 25 (2009) 587.
- [12] A. M. García-Campaña, W. R. G. Baeyens (Eds.), *Chemiluminescence in Analytical Chemistry*, Marcel Dekker, New York, NY, USA, 2001.
- [13] S. Beck, T. O’Keeffe, J. M. Coull, H. Köster, *Nucleic Acids Research* 17 (1989) 5115.
- [14] X.-H. Xu, A. J. Bard, *J. Am. Chem. Soc.*, 117 (1995) 2627.
- [15] Z. Chang, J. Zhou, K. Zhao, N. Zhu, P. He, Y. Fang, *Electrochimica Acta* 52 (2006) 575.
- [16] T. G. Mackay, A. Lakhtakia, *Opt. Express* 15 (2007) 14689. Erratum: 16 (2008) 3659.
- [17] T. G. Mackay, A. Lakhtakia, *J. Nanophotonics* 4 (2010) 041535.
- [18] R. Messier, T. Takamori, R. Roy, *J. Vac. Sci. Technol.* 13 (1976) 1060.
- [19] J. R. Blanco, P. J. McMarr, J. E. Yehoda, K. Vedam, R. Messier, *J. Vac. Sci. Technol. A* 4 (1986) 577.
- [20] F. Walbel, E. Ritter, R. Linsbod, *Appl. Opt.* 42 (2003) 4590.
- [21] J. A. Sherwin, A. Lakhtakia, I. J. Hodgkinson, *Opt. Commun.* 209 (2002) 369.
- [22] A. Lakhtakia, *Optik* 112 (2001) 145. Erratum: 112 (2001) 544.
- [23] T. G. Mackay, *Waves Random Media* 14 (2004) 485. Erratum: *Waves Random Complex Media* 16 (2006) 85.
- [24] A. Lakhtakia, W. S. Weiglhofer, *IEE Proc.–Microw. Antennas Propag.* 144 (1997) 57.
- [25] M. Born, E. Wolf, *Principles of Optics*, 7th ed., Pergamon, Oxford, UK, 1999, Appendix III.
- [26] F. Wang, *Int. J. Electron. Commun. (AEÜ)* 59 (2005) 258.
- [27] I. Hodgkinson, Q. h. Wu, J. Hazel, *Appl. Opt.* 37 (1998) 2653.
- [28] F. Chiadini, A. Lakhtakia, *Microw. Opt. Technol. Lett.* 42 (2004) 72.
- [29] L. Tsang, J. A. Kong, *Radio Sci.* 16 (1981) 303.
- [30] T. G. Mackay, A. Lakhtakia, W. S. Weiglhofer, *Phys. Rev. E* 64 (2001) 066616.
- [31] M. T. Prinkey, A. Lakhtakia, B. Shanker, *Optik* 96 (1994) 25.
- [32] B. Shanker, A. Lakhtakia, *J. Phys. D: Appl. Phys.* 26 (1993) 1746.
- [33] B. Shanker, *J. Phys. D: Appl. Phys.* 29 (1996) 281.
- [34] J. Van Kranendonk, J. E. Sipe, *Prog. Optics XV* (1977) 245.

- [35] M. D. Pickett, A. Lakhtakia, J. A. Polo Jr., *Optik* 9 (2004) 393.
- [36] B. Michel, A. Lakhtakia, W. S. Weiglhofer, *Int. J. Appl. Electromag. Mech.* 9 (1998) 167. Erratum: 10 (1999) 537.
- [37] T. G. Mackay, *J. Nanophotonics* 2 (2008) 021850.

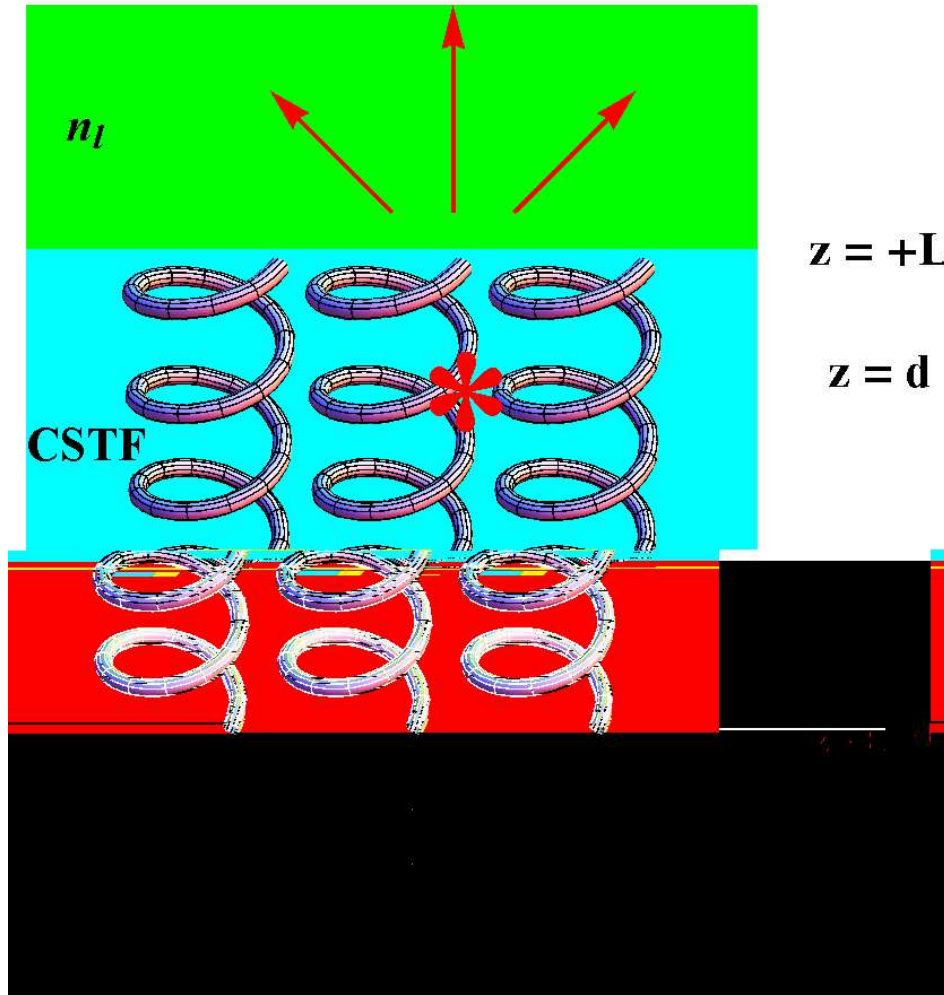


Figure 1: A schematic diagram of the scenario under investigation: radiation emitted from a dipole source embedded within an infiltrated CSTF occupying $-L < z < L$.

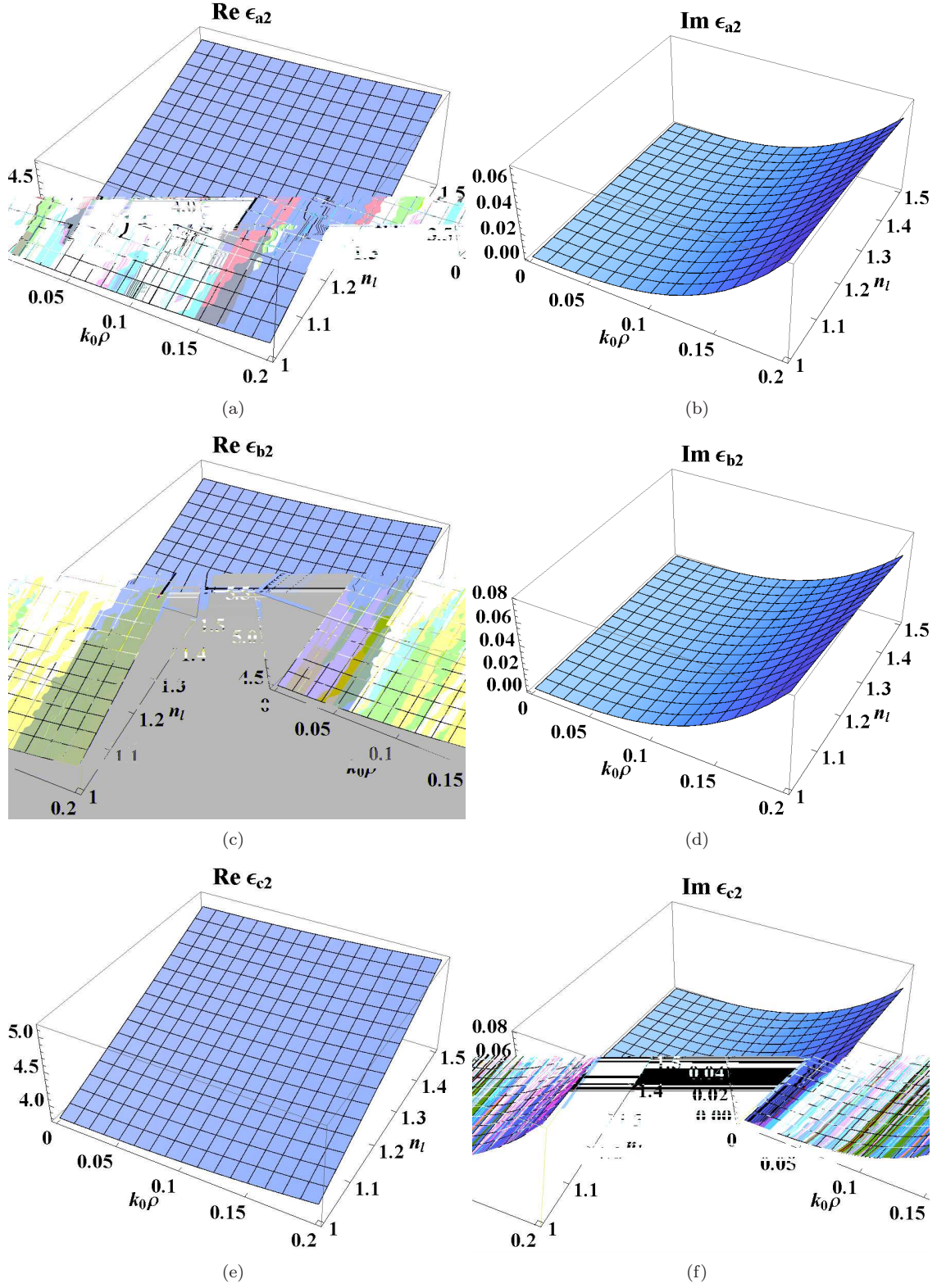


Figure 2: Real and imaginary parts of the relative permittivity parameters ϵ_{a2} , ϵ_{b2} and ϵ_{c2} versus refractive index $n_\ell \in (1, 1.5)$ and relative size parameter $k_0 \eta \in (0, 0.2)$.

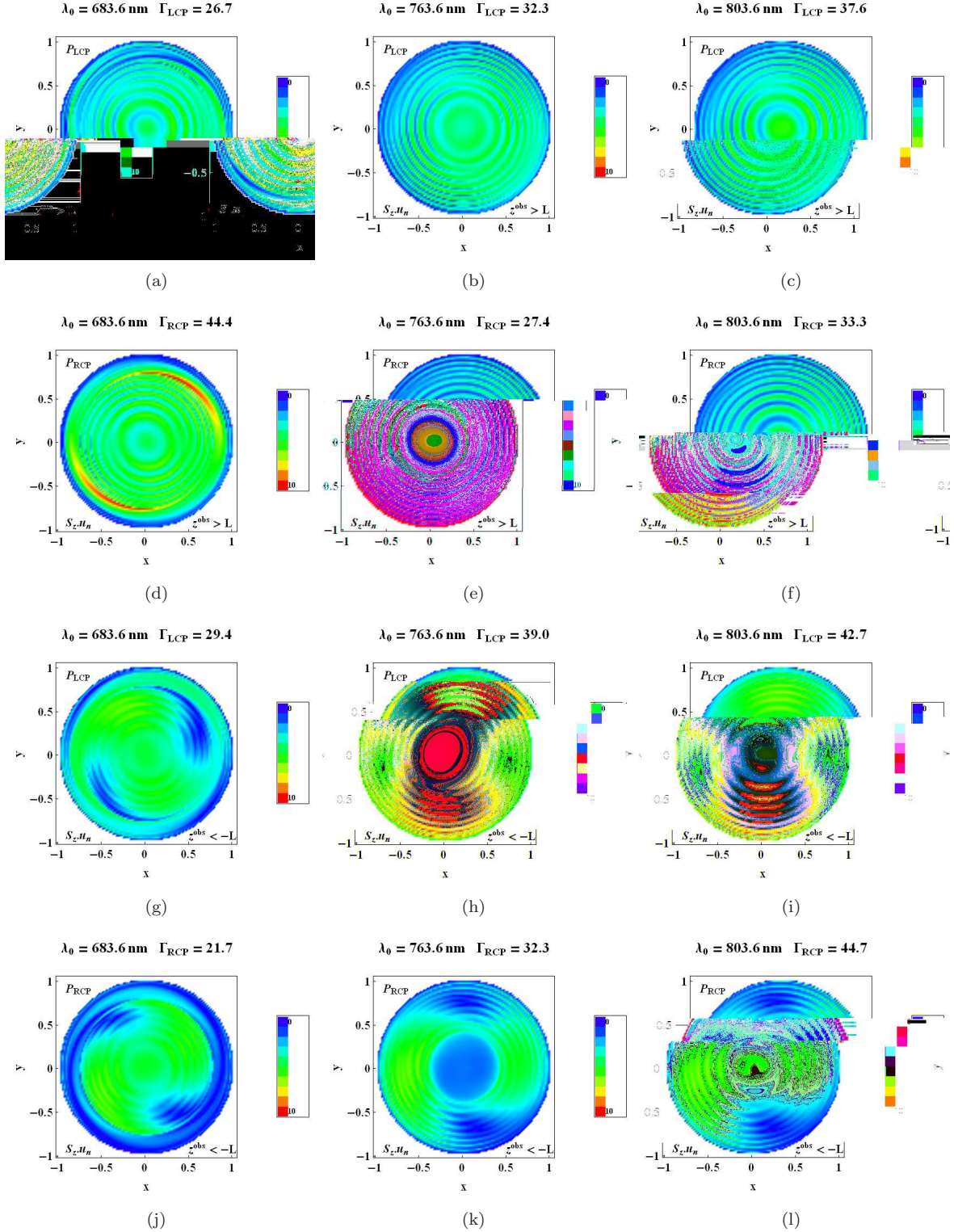


Figure 3: Projections of $|P_{LCP}|$ and $|P_{RCP}|$ (scaled by $10^{13}\omega^{-2}|p|^{-2}$) onto the $z = 0$ plane for $z^{obs} > L$ and $z^{obs} < -L$. Here $\lambda_0 \in \{683.6\text{nm}, 763.6\text{nm}, 803.6\text{nm}\}$ and $n_\ell = 1.0$.

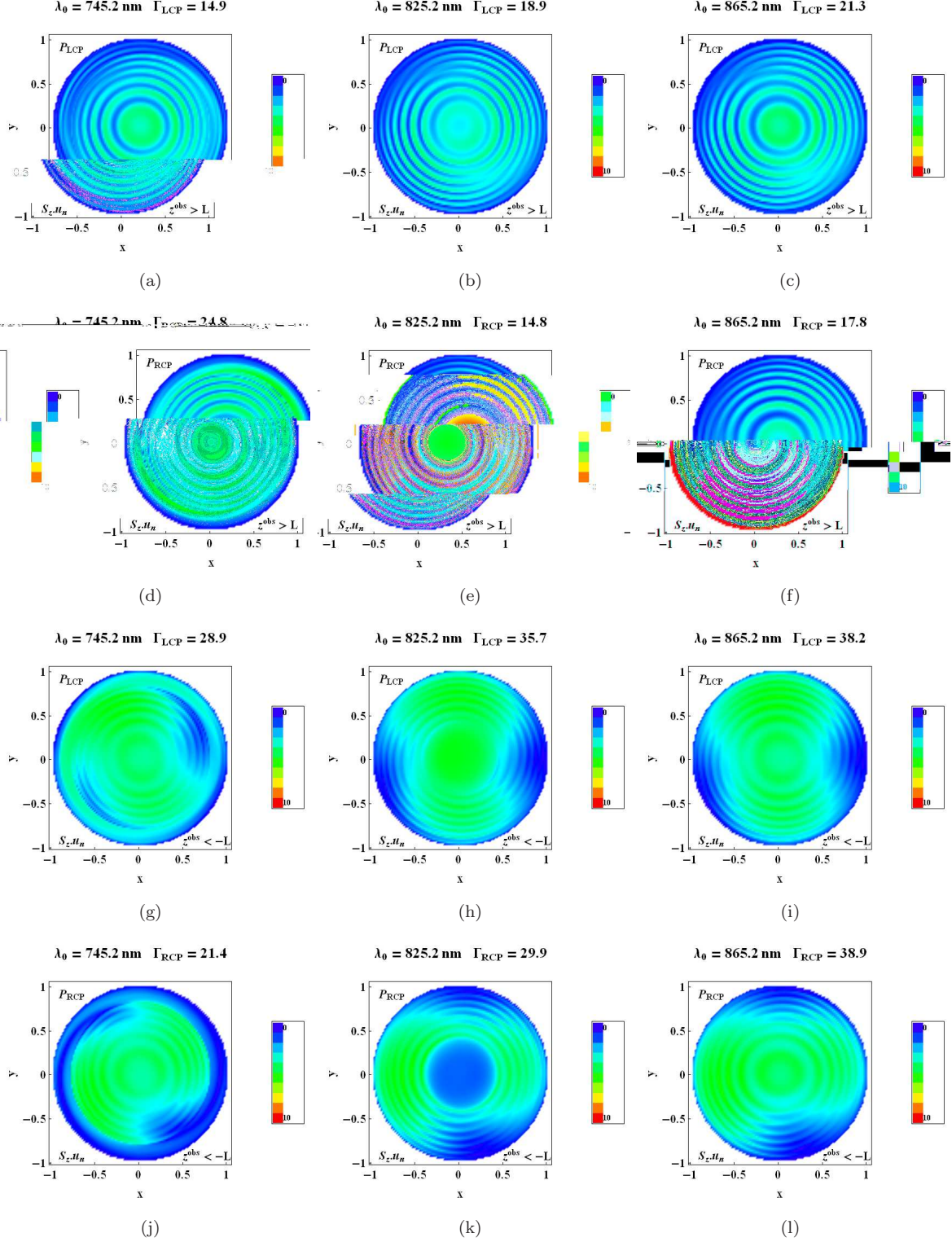


Figure 4: As Fig. 3 but with $\lambda_0 \in \{745.2\text{nm}, 825.2\text{nm}, 865.2\text{nm}\}$ and $n_l = 1.25$. The relative permittivity parameters $\{\epsilon_{a2}, \epsilon_{b2}, \epsilon_{c2}\}$ for the infiltrated CSTF were computed using the non-extended version of the Bruggeman homogenization formalism.

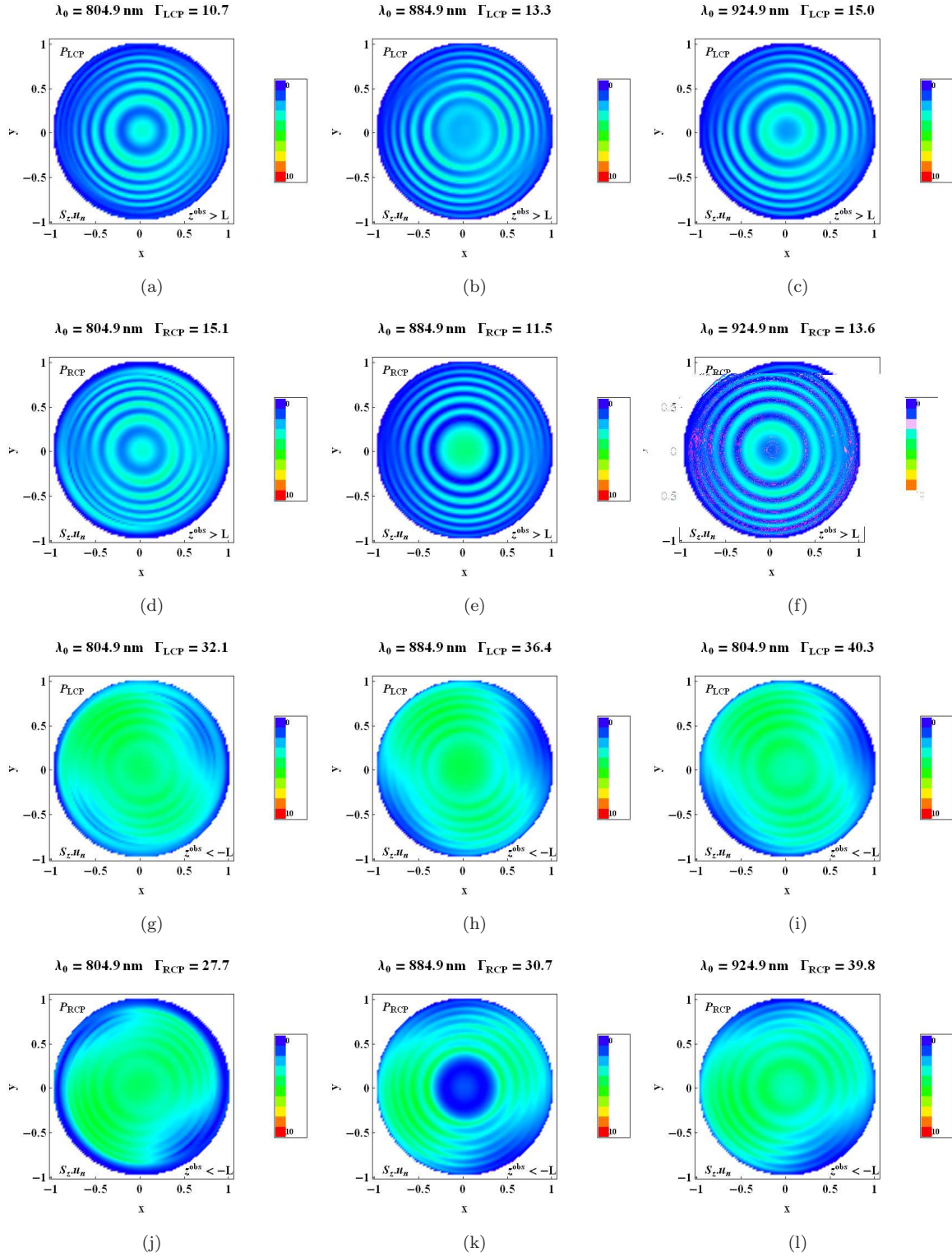
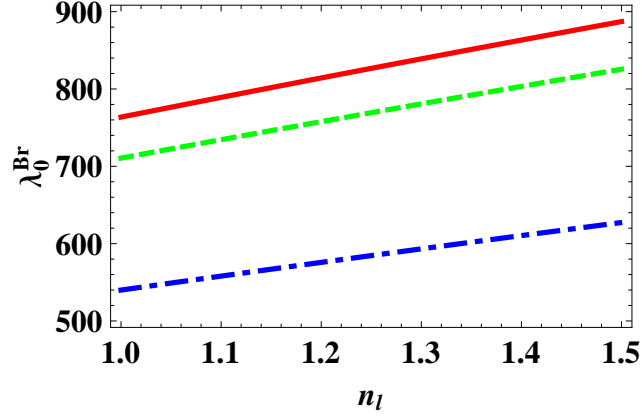
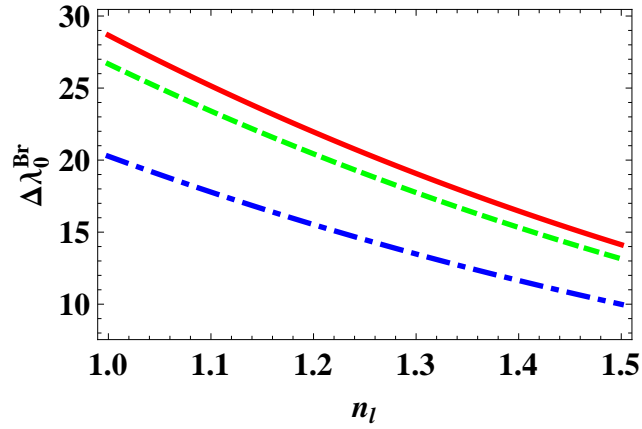


Figure 5: As Fig. 4 but with $\lambda_0 \in \{804.9\text{nm}, 884.9\text{nm}, 924.9\text{nm}\}$ and $n_l = 1.5$.



(a)



(b)

Figure 6: λ_0^{Br} and $\Delta\lambda_0^{Br}$ plotted against n_l for $\theta^{obs} = 0^\circ$ (solid, red curve), $\theta^{obs} = 30^\circ$ (dashed, green curve) and $\theta^{obs} = 60^\circ$ (broken dashed, blue curve). The relative permittivity parameters $\{\epsilon_{a2}, \epsilon_{b2}, \epsilon_{c2}\}$ for the infiltrated CSTF were computed using the non-extended version of the Bruggeman homogenization formalism.

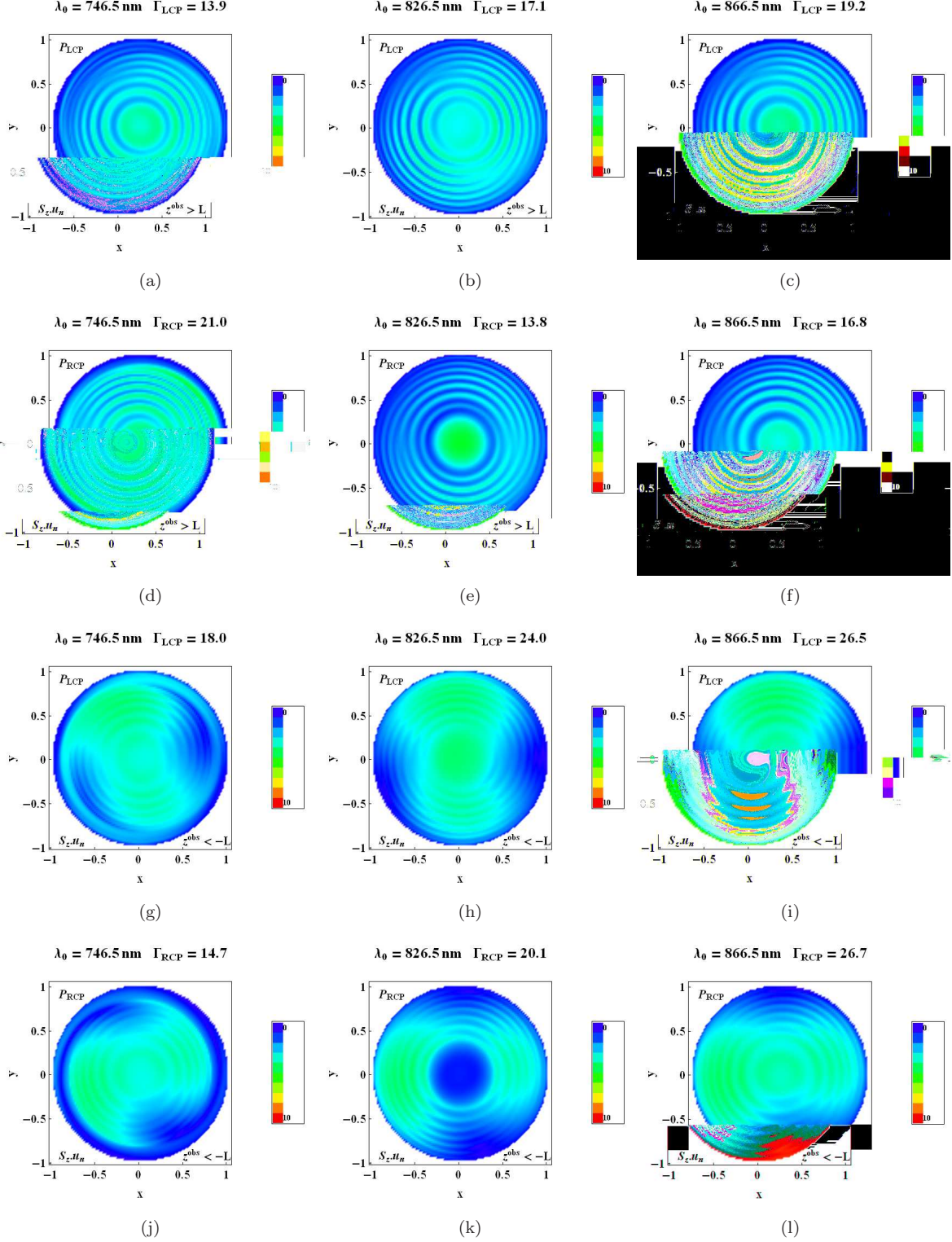
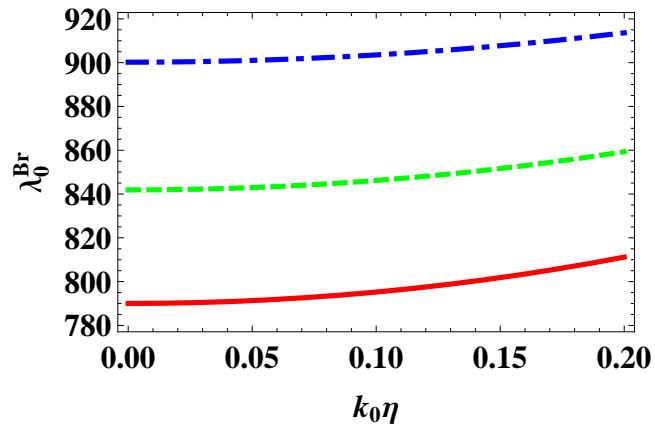
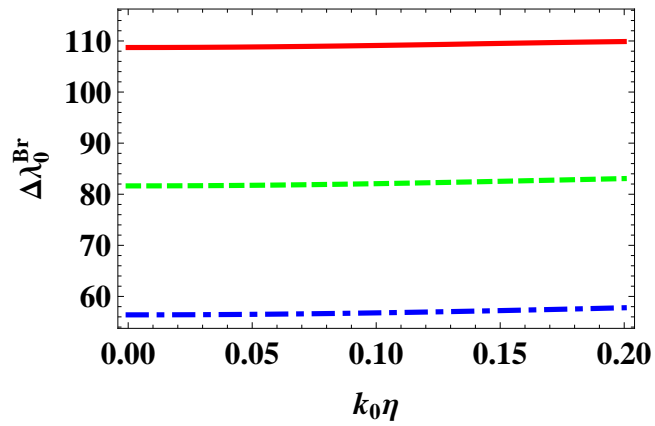


Figure 7: As Fig. 4 but the relative permittivity parameters $\{\epsilon_{a2}, \epsilon_{b2}, \epsilon_{c2}\}$ for the infiltrated CSTF were computed using the extended version of the Bruggeman homogenization formalism with $\eta = 0.1/k_0$, and $\lambda_0 \in \{746.5\text{nm}, 826.5\text{nm}, 866.5\text{nm}\}$.



(a)



(b)

Figure 8: λ_0^{Br} and $\Delta\lambda_0^{Br}$ plotted against $k_0\eta$ for $n_\ell = 1.0$ (solid, red curve), $n_\ell = 1.25$ (dashed, green curve) and $n_\ell = 1.5$ (broken dashed, blue curve), as computed using the extended Bruggeman homogenization formalism. The angle $\theta^{obs} = 0^\circ$.